JOURNAL OF PROPULSION AND POWER
Vol. 24, No. 1, January–February 2008

Near Exit Plane Velocity Field of a 200-Watt Hall Thruster

William A. Hargus Jr.* and Christopher S. Charles†
U.S. Air Force Research Laboratory, Edwards Air Force Base, California 93524

DOI: 10.2514/1.29949

This work presents the near exit plane velocity field of a 200-W laboratory xenon Hall thruster at a single operating condition with a 250-V anode potential. The ionized propellant velocities were measured using laser-induced fluorescence of the $5d[4]_{7/2} - 6p[3]_{5/2}$ excited state xenon ionic transition at 834.72 nm. Ion velocities were interrogated from the acceleration channel exit plane to a distance 107 mm from the exit plane (3.3 exit plane diameters). Both axial and radial velocities were measured. A nearly uniform axial velocity profile of approximately 13,800 ± 500 m/s (130 ± 10 eV) was measured at the thruster exit plane. The maximum axial velocity, measured 107 mm from the exit plane, was 16,800 m/s (192 eV). The ion flow exiting the thruster acceleration channel mixes downstream due to both the coaxial thruster geometry and a possible ion-acoustic shock. This behavior appears in regions where multiple, or broadly distributed, radial and axial velocity components occur. These regions also exhibit broadened fluorescence line shapes, likely indicative of collisions between the various velocity populations as well as possible ionization of background neutral, and correspond to the brighter, more visible portions of the plume. This region has been previously identified as a possible ion-acoustic shock. This hypothesis appears consistent with the low radial velocity ion populations measured in this more luminous portion of the plume. In addition, a limited study at five off-nominal conditions near a region of high insulator erosion indicates that the impinging ion energy on the protruding center pole boron nitride insulator is predictably changed by flow rates and anode potentials; however, it also appears to vary significantly with applied magnetic field strength.

Introduction

TO BETTER characterize the use of Hall thrusters for on-orbit applications, there is a need for improved understanding of the near exit plane ion velocity field. Spacecraft interaction models have been developed that use near exit plane plasma information to estimate plume divergence and interactions with spacecraft surfaces [1]. A major limitation of these models is the accuracy of available near exit plane plume data. This is compounded by external ion acceleration due to small external electric fields.

This study seeks to characterize the near plume velocity field of a 200-W Hall thruster using excited state ionic xenon laser-induced fluorescence (LIF). LIF is a preferred diagnostic for the investigation of plasma in the near plume regions because it is a nonintrusive measurement. Unlike electrostatic probes, LIF will not perturb the local plasma or thruster operation.

Xenon Ion Spectroscopy

The nine stable isotopes of xenon, the propellant most commonly used in Hall thrusters due to its high atomic mass (131.3 amu) and low ionization energy (12.1 eV), each have a slight difference in their electron transition energies due to their mass differences. The odd mass isotopes are further spin split due to nuclear magnetic dipole and electric quadrapole moments. Nuclei which have an odd number of protons and/or an odd number of neutrons possess an intrinsic nuclear spin $Ih/2\pi$ where I is integral or half-integral depending on whether the atomic mass is even or odd, respectively. For nuclei with nonzero nuclear spin (angular momentum), there exists an interaction of the nucleus with the electron shell. This interaction leads to the splitting of levels with angular momentum J into a number of components, each corresponding to a specific value of the total angular momentum F. The details of how this hyperfine spin splitting affects the spectra of xenon, and in particular with regard to the transition studied in this work, are described in more detail elsewhere [2].

For the results reported here, we probed the 834.72 nm electronic transition of singly ionized xenon. The isotopic and nuclear-spin effects contributing to the hyperfine structure of the $5d[4]_{7/2} - 6p[3]_{5/2}$ xenon ion transition have a total of 19 isotopic and spin split components. The hyperfine splitting constants, which characterize the variations in state energies, are only known for a limited set of energy levels. Unfortunately, the 834.72 nm xenon ion transition only has data on the nuclear-spin splitting constants of the $6p[3]_{5/2}$ upper state, and no information is available on the transition dependent isotope shifts [3–5]. This makes modeling of the line shape somewhat speculative.

For velocity measurements, it is often convenient to probe optically accessible transitions for which there is incomplete knowledge of the isotopic and nuclear-spin splitting constants. Manzella and others have previously used the $5d[4]_{7/2} - 6p[3]_{5/2}$ xenon ion transition at 834.72 nm to make velocity measurements in a Hall thruster plume [2,6–8]. A convenient feature of this transition is the presence of a relatively strong line originating from the same upper state ($6s[2]_{3/2} - 6p[3]_{5/2}$ transition at 541.9 nm [9]) which allows for nonresonant fluorescence collection. A nonresonant fluorescence scheme is preferred where there is the possibility of laser scattering from surfaces. Several others have also used the $5d[3]_{7/2} - 6p[2]^0_{5/2}$ xenon ion transition at 605.1 nm, for which all the nuclear-spin splitting constants are known, to perform similar measurements [10,11]. However, this transition is both considerably broader and less accessible using inexpensive diode lasers.

A local velocity is determined by the spatially resolved measurement of the Doppler shift of the absorbing ions. If an absorber has a velocity component along the axis of the laser beam, it will absorb the light at a frequency shifted from that of stationary absorbers. The magnitude of this frequency shift $\Delta\upsilon_{12}$ depends on the speed u of the absorbing population along the laser beam axis

$$\Delta\upsilon_{12} = \upsilon_{12}\frac{u}{c} \tag{1}$$

where c is the speed of light. The Doppler shift $\Delta\upsilon_{12}$ of a species' fluorescence profile away from the line center υ_{12} of stationary absorbers is in proportion to u [12].

Received 23 January 2007; revision received 30 July 2007; accepted for publication 23 August 2007.

*Research Engineer, Spacecraft Propulsion Branch. Senior Member AIAA.
†Physicist, Spacecraft Propulsion Branch. Member AIAA.

Table 1 Nominal Thruster Operating Conditions

Parameter	Measurement
Anode flow	840 μg/s Xe
Cathode flow	98 Mg/s Xe
Anode potential	250 V
Anode current	0.82 A
Keeper current	0.0 A
Magnet current	1.0 A
Heater current	0.0 A

Apparatus

The measurements we present in this work were performed in chamber 6 at the U.S. Air Force Research Laboratory (AFRL) Electric Propulsion Laboratory at Edwards Air Force Base, California. Chamber 6 is a nonmagnetic stainless steel chamber that has a 1.8 m diameter and 3.0 m length. It has a measured pumping speed of 32, 000 l/s on xenon. Pumping is provided by four single-stage cryogenic vacuum panels (single-stage cold heads at $\sim$25 K) and one 50 cm two-stage cryogenic vacuum pump ($\sim$12 K). Chamber pressure during thruster operation is approximately 6.7×10^{-4} Pa, corrected for xenon.

The thruster used for this test is the Busek Company, Inc. BHT-200-X3 200-W Hall thruster which has been described elsewhere [13]. Table 1 shows the typical operating conditions for the Hall thruster. During thruster operation, the parameters shown in Table 1 are monitored and recorded at a 1 Hz data rate.

Figure 1 shows a side-view diagram of the Hall thruster mounted in the vacuum chamber. The thruster is mounted on a three-axis orthogonal computer-controlled translation system. Figure 1 also shows the two orthogonal LIF probe beams and windows through which the beams enter the chamber. Figure 2 shows a top view of the laser optical train, collection optics, and one leg of the external probe optics.

The laser used is a New Focus Vortex tunable diode laser. It is capable of tuning approximately $\pm$50 GHz about a center wavelength of 834.72 nm. The 10 mW beam is passed through a Faraday rotator to eliminate feedback to the laser. The laser beam then passes through several beam pickoffs until it reaches a 50-50 beam splitter (BS) where it is split into two beams of equal power. The first beam, the axial probe beam shown in Figs. 1 and 2, is focused by a lens and enters the vacuum chamber through a window. A second probe beam, shown in Fig. 2 only, is directed from the optical bench via a periscope apparatus so that it enters the chamber from above the thruster and probes the velocity perpendicular to the first probe beam. Each probe beam is chopped at a unique frequency by choppers Ch2 (2 kHz) and Ch3 (2.8 kHz) for phase sensitive detection of the fluorescence signals.

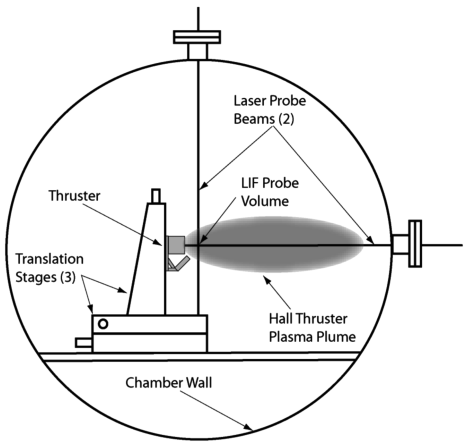

Fig. 1 Side-view diagram of thruster within the vacuum chamber. Also shown are the translation stages and the laser probe beams.

The two wedge beam splitters (BS) shown in Fig. 2 provide portions of the beam for diagnostic purposes. The first beam pickoff directs a beam to a photodiode detector (D1) used to provide constant power feedback to the laser. The second beam is divided into two equal components by a 50-50 beam splitter cube. The first component is directed to a Burleigh WA-1500 wavemeter used to monitor absolute wavelength. The second component is sent through chopper Ch1 (1.3 kHz) and through a low-pressure xenon hollow cathode discharge lamp. The lamp provides a stationary absorption reference for the determination of the Doppler shift $\Delta\upsilon_{12}$. Unfortunately, the hollow cathode lamp produces no detectable population of the ionic xenon $5d[4]_{7/2}$ state. However, there is a nearby (18.1 GHz distant) neutral xenon $6s[1/2]^0_1 - 6p'[3/2]_2$ transition at 834.68 nm [14,15]. Absorption of this neutral xenon transition provides a stationary reference for measurement of the Doppler shifted ionic transition. The second pickoff sends a beam to a 300 MHz free spectral range Fabry–Perot etalon (F-P). This instrument provides high-resolution frequency monitoring of the wavelength interval swept during a laser scan.

The fluorescence collection optics are also shown in Fig. 2. The fluorescence signal is collected by a 75-mm-diam, 300 mm focal length lens within the vacuum chamber. The collimated signal is directed through a window in the chamber sidewall to a similar lens that focuses the collected fluorescence onto the entrance slit of 125 mm focal length monochrometer with a Hamamatsu R928 photomultiplier tube (PMT) detector. Because of the 1:1 magnification of the collection optics, the spatial resolution of the measurements is determined by the geometry of the entrance slit 1 mm width and 1.7 mm height.

The laser is controlled by an analog ramp signal generated by a data acquisition system. During each laser scan, the data acquisition card records the absorption and two fluorescence signals using three lock-in amplifiers. The signal from the Fabry–Perot etalon photodiode detector (D3) signal is amplified and filtered using a current preamplifier, the output of which is also recorded. Typically, the scans span 55 GHz. Each scan yields four traces of several thousand points. The traces are then stored for postprocessing.

Figure 3 shows the near-field geometry of the Hall thruster. The locations of the central magnetic pole nose cone and edges of the acceleration channel are indicated as is the position of the cathode exit. The Cartesian coordinate system and origin used in these measurements are also shown in Fig. 3. The origin is at the tip of the

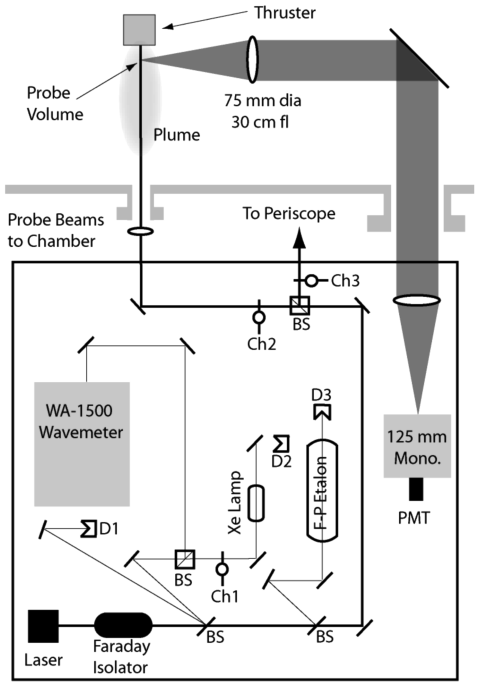

Fig. 2 Top-view diagram of the laser optical train and collection optics.

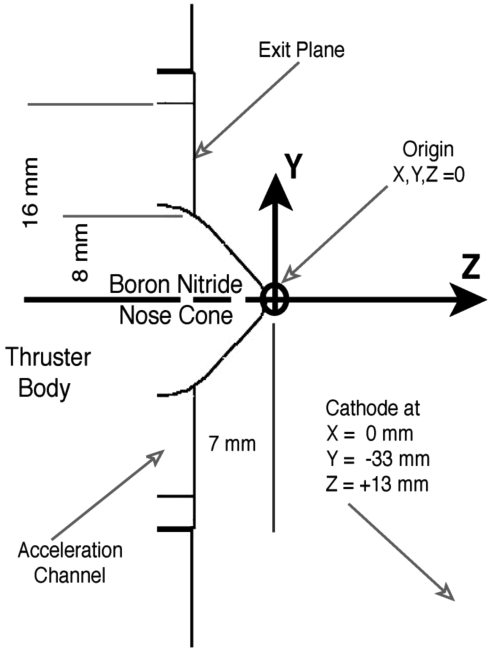

Fig. 3 Near-field dimensions of the Hall thruster with origin of the coordinate system and positions of important locations noted.

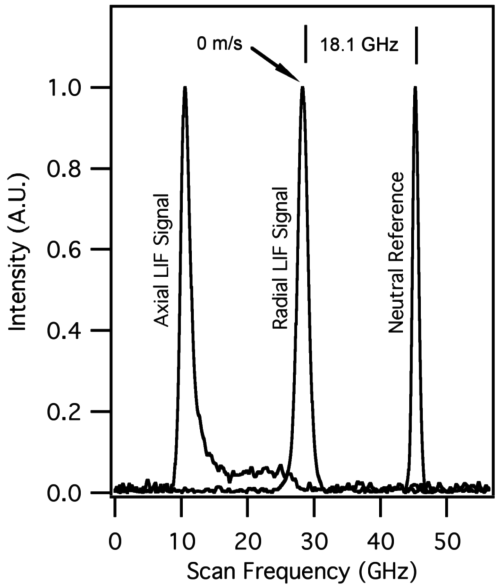

Fig. 4 Sample LIF/absorption trace. This particular trace was taken at the exit plane in the center of the acceleration channel ($Y = 12$, $Z = -7$ mm).

nose cone due to the ease and repeatability with which this position may be located. All measurements presented in this work will be identified using these coordinates. Furthermore, measurements presented in this work will be limited to the Y–Z plane.

Experimental Results

Figure 4 shows a sample LIF/absorption trace used to determine the velocity components of accelerated xenon ions (center of upper exit plane, $Y = 12$ mm, $Z = -7$ mm). The peak on the right-hand side of the figure is the neutral $6s[1/2]_1^0 - 6p'[3/2]_2$ transition absorption trace, rectified for clarity. At 18.1 GHz to the left is the position at which the ion $5d[4]_{7/2} - 6p[3]_{5/2}$ transition fluorescence would appear if the interrogated plasma were stationary. The left peak is the fluorescence signal extracted from the probe beam parallel to the Z axis (axial). The center peak is the signal from the probe beam parallel to the Y axis (radial because $X = 0$ for all measurements presented). In this case, the axial plasma velocity is $13,800$ m/s and the radial velocity is -900 m/s. The length of the probe beam over which the velocities are averaged is 1 and 1.7 mm for the axial and radial measurements, respectively.

The uncertainty is estimated to be ± 500 m/s due to several factors. The first issue is the uncertainty in the relative neutral and ionic transition energies. The second issue concerns the resultant fluorescence line shapes. Figure 4 initially shows a reasonably sharply peaked fluorescence line shape. However, closer examination reveals a distinct low-velocity component in the axial component. The fluorescence line shapes measured in this study indicate the ion velocity is not a simple shifted Maxwell–Boltzmann distribution. Rather, it is a convolution of a sometimes complex distributed velocity distribution with the transition line shape.

In this study, we have chosen to identify the peaks of the fluorescence line shapes as the local velocities. In the mixing portions of the flow, there is often more than one recognizable velocity population. In these cases, the distinct peaks are each assigned a velocity. In all these cases, the peaks are within the quoted uncertainty of ± 500 m/s or better. In fact, the repeatability of the peak locations appears to be a fraction of the quoted uncertainty (± 80 m/s). However, the fluorescence line shapes are often significantly broadened, presumably due to wide velocity distributions. The quoted uncertainty should therefore be viewed as the uncertainty in the determination of the peak of the fluorescence line shape. In most cases, this will correspond to the velocity of the majority of the ion population. When multiple velocities are given for a single location, there may be ions with intermediate velocities. It should also be noted that there exists some uncertainty in the precise separation between the ion and neutral transitions and this also represents another potential source of measurement uncertainty.

Figures 5 and 6 show the velocity field measured in this study for the nominal operating conditions specified in Table 1. As shown in Fig. 5, the ions diverge as they emerge from the acceleration channel of the thruster. The ions are externally accelerated axially and continue to diverge, particularly near the thruster nose cone. Beyond the nose cone, the most striking feature of the flowfield is the appearance of the mixing of distinct ion velocity populations that originate from opposite sides of the nose cone, as well as the appearance of a low radial velocity population. This mixing of divergent velocity populations begins near the nose cone tip ($Z = 0$ mm), but appears most noticeably near the cathode plane ($Z = 13$ mm). Further downstream, the divergent flows produce a central core with low radial velocities. This core is in turn surrounded by a sheath where there appears to be more than one velocity population. The sheath occurs where there is a broad distribution within the radial velocity distribution. This may be consistent with a region in which large numbers of ion collisions occur. Furthermore, these regions correspond with the visible plume jet typically exhibited by Hall thrusters and have tentatively been identified as an ion-acoustic shock [13].

Figure 7 shows the velocity profile at the thruster exit plane. The axial velocity component is approximately uniform at $13,800$ m/s (130 ± 10 eV). The radial velocity varies continuously from 3500 to -6000 m/s ($\sim$8 to 25 eV). The flow is approximately symmetrically divergent about the center of the acceleration channel ($Y = 12$ mm), however, the greatest radial velocity occurs nearest the boron nitride nose cone covering the central magnetic pole.

Figure 8 shows a cross section of the velocity field at 3 mm beyond the tip of the nose cone ($Z = 3$ mm). Here, the axial velocity has increased to a maximum of $16,500$ m/s ($\sim$185 eV), but is no longer cross-sectionally uniform. The dip about the thruster centerline ($Y = 0$) may be caused by the flow of ions around the nose cone. The radial velocities peak at nearly $\pm 10,000$ m/s (68 eV) and are, as would be expected, symmetric about the thruster centerline. At this axial location, the majority of the energy has been electrostatically deposited into the ions.

At the cathode plane ($Z = 13$ mm), the velocity profile in Fig. 9 looks similar to that seen previously in Fig. 8. In Fig. 9, the propellant has not been accelerated significantly past the previous maximum of nearly $16,500$ m/s. However, two features are of interest. First, the

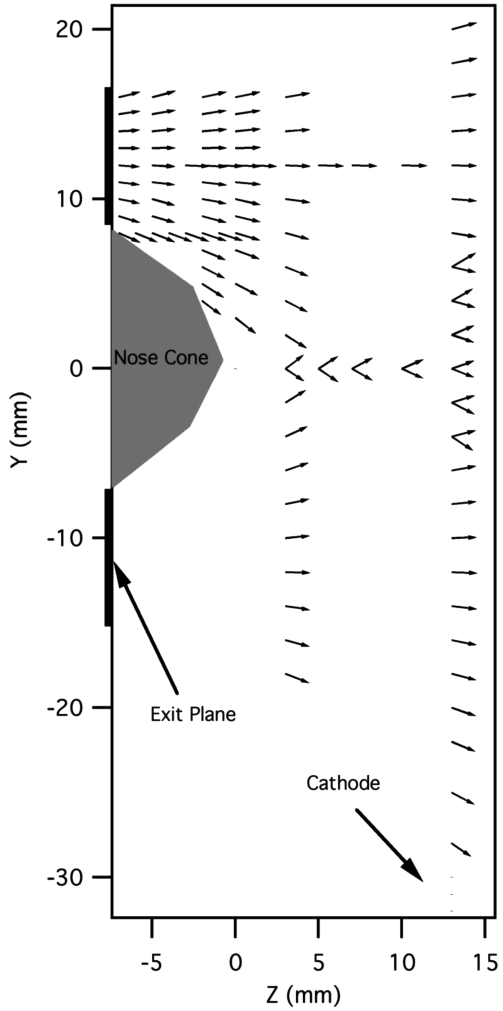

Fig. 5 Near exit plane velocity vector field for the operating conditions specified in Table 1.

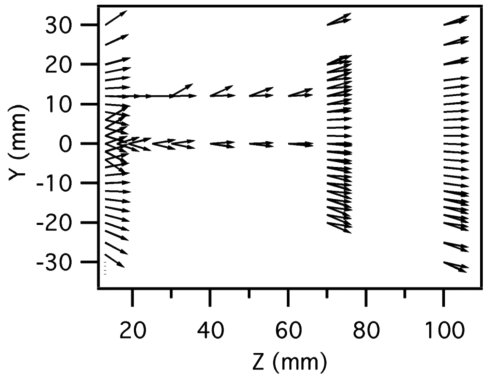

Fig. 6 Velocity vector field beyond the cathode plane for the conditions specified in Table 1.

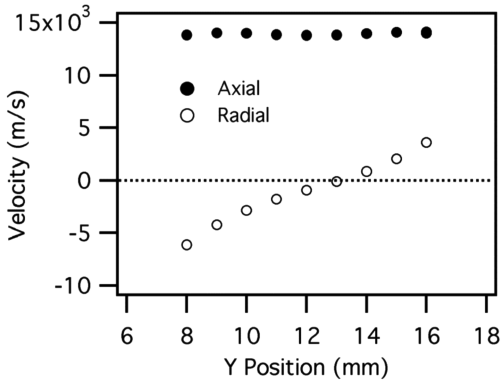

Fig. 7 Exit plane ($Z = -7$ mm) velocity field. Note the divergence, especially toward the central magnetic pole at $Z = 0$.

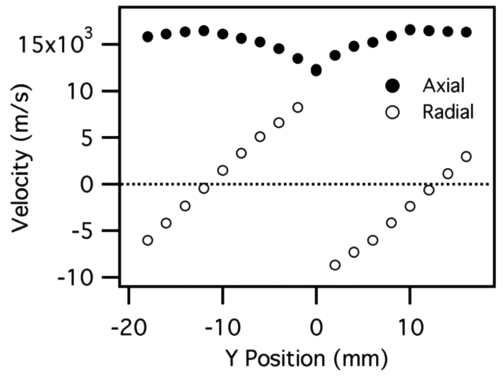

Fig. 8 Velocity field 3 mm beyond the nose cone, ($Z = 3$ mm). Note the symmetrical divergence and the turning of the flow around the thruster nose cone.

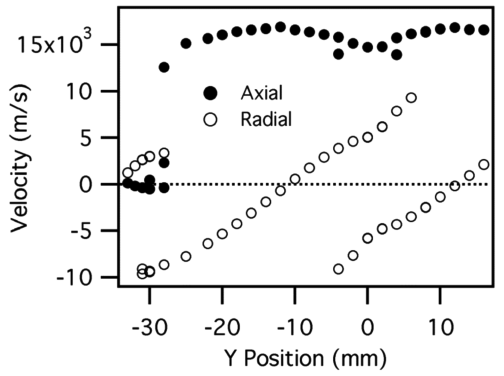

Fig. 9 Velocity field at cathode plane 13 mm beyond the nose cone, ($Z = 13$ mm).

flow from the cathode produces low ion velocities near the cathode exit. Second, the mixed flow regime is larger. In addition to the multiple radial velocity components, several locations have multiple axial velocity components. A more subtle change from the previous velocity profile is a slight flattening of the axial velocity profile. It should be noted that although the multiple radial velocity components are denoted here as single points, they often contain broader fluorescence profiles than seen elsewhere in the plume.

The axial velocity profile continues to flatten, as shown in Fig. 10, at $Z = 100$ mm. The velocity of the axial velocity component has increased slightly, increasing the peak axial directed kinetic energy of the xenon ions to 192 eV (16, 800 m/s). The flow has evolved into a slightly divergent central flow surrounded by a sheath where mixing of more than one velocity group is also occurring. Because this position was the maximum axial distance examined, it is assumed that this characteristic behavior extends further downstream.

Profiles of the external acceleration of the xenon ions are shown for two radial locations in Figs. 11 and 12. Figure 11 shows the ion axial and radial velocity components starting at the center of the upper acceleration channel ($Y = 12$ mm) from the exit plane to $Z = 100$ mm. Figure 12 shows the velocity components at the centerline of the thruster ($Y = 0$) beginning at the tip of the nose cone ($Z = 0$). These two figures show some interesting features of the Hall thruster plume dynamics.

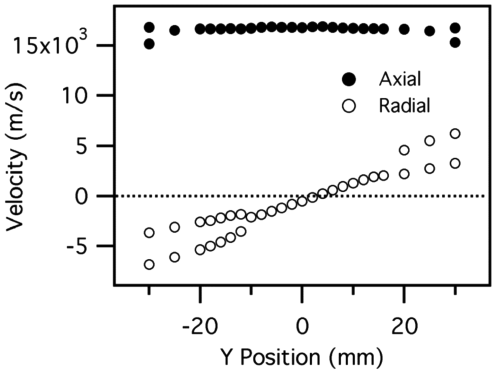

Fig. 10 Velocity field at $Z = 100$. Note the development of a flattened axial velocity distribution and the multiple velocity vectors in the plume periphery.

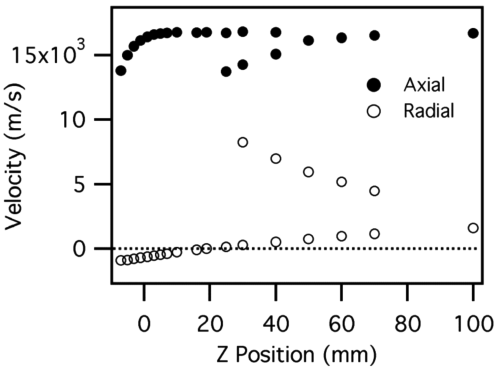

Fig. 11 Velocity profile at center of the acceleration channel ($Y = 12$ mm) from exit plane ($Z = -7$ mm) to $Z = 100$ mm.

Figure 11 illustrates the extent of the acceleration occurring outside the thruster acceleration channel by following the velocity components along the acceleration channel center ($Y = 12$ mm) from the exit plane ($Z = -7$ mm) to $Z = 100$ mm. The propellant exits the thruster at approximately 13,800 m/s and accelerates to a maximum axial velocity of 16,800 m/s. The propellant ions gain approximately 58 eV in this process. At this radial location, the first evidence of mixing velocity groups appears at $Z = 25$ mm. At approximately $Z = 50$ mm, the multiple axial peaks can no longer be separated. The apparent drop in axial velocity at this location is an artifact of this issue and should not be construed as actual deceleration of the xenon ions. Rather, it is an average velocity of the two velocity populations that have been thoroughly mixed.

Figure 12 provides an alternative view of the external acceleration. Here we see the acceleration starting at the nose cone ($Z = 0$) and extending to $Z = 100$ mm. The extent of the acceleration in Fig. 12 is less than in Fig. 11 because the start point is 7 mm further downstream. The initially lower velocities in Fig. 12 are due to the distance required for radial ion diffusion to populate the plume core. The diffusion manifests itself in Figs. 8–10, which exhibit increasingly shallow gull-wing axial velocity component profiles. The apparently immense axial acceleration near the nose cone ($Z = 0$) is due to a population of slow-moving ions located in the lee of the nose cone. Although the mean velocity at this location is approximately zero, the fluorescence line shape is very broad at this location. The xenon ions at this location appear to have a broadly distributed velocity distribution. Physical evidence of high-energy ions at this location possessing negative axial velocity is apparent from a pit formed at the nose cone tip, presumably due to sputtering of boron nitride due to ion bombardment. Figure 12 also shows the increasingly axial plume core flow. From the nose cone to approximately 70 mm, the central flow is dominated by a mixing of divergent radial flows. Beyond 70 mm, the flow along the plume centerline is nearly entirely axial with only small radial velocity components.

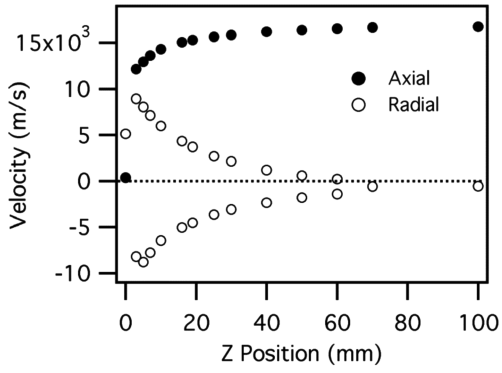

Fig. 12 Velocity profile at center of the thruster ($Y = 0$ mm) from tip of nose cone ($Z = 0$) to $Z = 100$ mm.

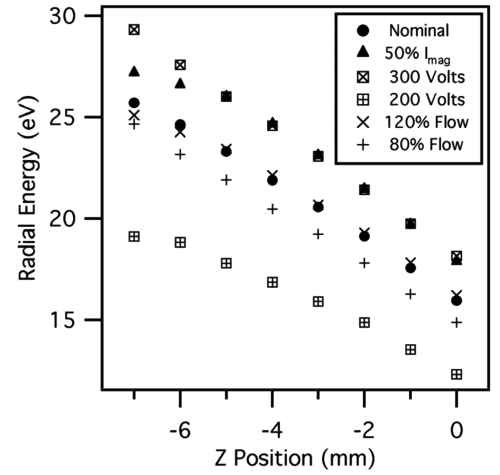

Fig. 13 Radial ion energies at $Y = 8$ mm for a range of Z locations for six operating conditions.

An extension to the measurements at the nominal operating conditions presented in Table 1 is shown in Fig. 13. Here, we show the radial energies calculated from radial velocity measurements directed toward the nose cone at $Y = 8$ mm from the exit plane to the tip of the nose cone. Six distinct operating conditions are shown: the nominal condition and five off-nominal conditions. These off-nominal conditions include decreased magnetic field strength, increased/decreased discharge voltage, and increased/decreased anode flow.

Erosion of the nose cone is a possible life-limiting mechanism. Erosion is dependent on both the energy and flux of the impacting ions as well as the impact angle. Figure 13 hints at the changes in relative erosion rate at the nose cone likely to occur by operation at conditions other than those shown in Table 1. As would be expected, the data are bracketed by operation at the high- and low-discharge potentials (300 and 200 V vs a nominal 250 V). Most interesting is the significant increase of ion radial energy exhibited by operation at a reduced magnetic current strength (0.5 A vs a nominal 1.0 A). In this case, the anode current did not rise significantly (840 mA vs a nominal 820 mA), however, the resultant decrease in thruster magnetic field increased the radial velocity component significantly. In fact, the flow angles for this case increased inward by approximately 2 deg at the nose cone base and 1 deg near the tip. Finally, it should be noted that the erosion rate is not only a function of the directed ion energy, but is also proportional to flux. It may be assumed that the ion flux is approximately increased in proportion to the anode flow rate. This is important in the examination of the two cases in Fig. 13 which vary the anode propellant flow rate.

Conclusions

The velocity field for the near plume region of a 200-W Busek BHT-200-X3 Hall thruster has been extensively mapped for a single

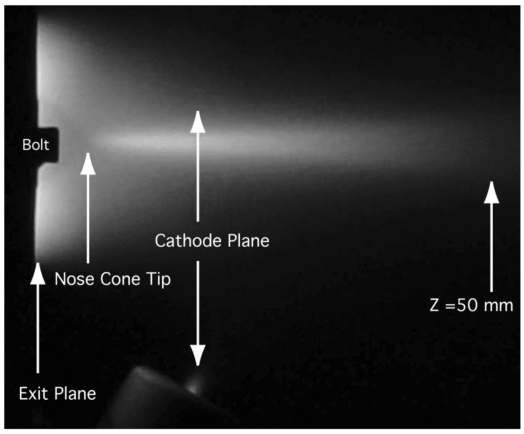

Fig. 14 Photograph of the BHT-200 Hall thruster plume operating at nominal conditions. Note similarities to vector fields presented in Figs. 5 and 6 as well as the velocity profile in Fig. 12.

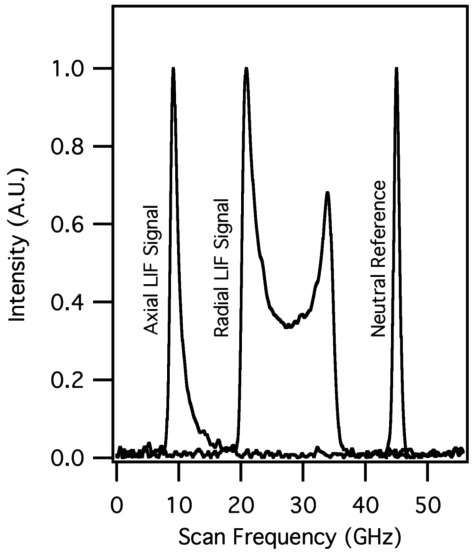

Fig. 15 Fluorescence and rectified absorption traces for $Y = 0$, $Z = 13$ mm. Note broadened bimodal radial fluorescence distribution.

operating condition as well as sampled for five additional operating conditions. The measurements indicate that approximately 130 eV ions emerge from the thruster. These ions are further accelerated to 185 eV between the exit plane and the cathode plane, and eventually reach a maximum axial directed energy near 192 eV. This is consistent with the 250 V acceleration potential. Previous measurements on other Hall thrusters have shown a difference of approximately 50 V between the maximum ion energy and discharge potential, and has been attributed to the combined anode and cathode falls [2].

The flowfield itself is shown to be complex with mixing of distinct velocity populations. The mixing behavior becomes significant beyond the tip of the central magnetic pole nose cone. Further downstream, at approximately 80 mm from the exit plane, the divergent flows produce a central core with a small radial velocity component. This core is in turn surrounded by a sheath where there appears to be more than one velocity population. This sheath appears to be related within the plume and is believed to correspond to the visible jet structure typically exhibited by Hall thruster plumes. The behavior of the central plume core appears to be due to the diffusion of the plume ions into the central core region, possibly due to a potential difference between the acceleration channel center and the thruster centerline. This is consistent with lines of equipotential following expected lines of magnetic flux. Such a plume plasma potential structure would inhibit low-energy ions within the central core from exiting. It would also direct the flow in a nearly parallel beam consistent with the measured axial core flowfield. This appears consistent with visual inspection of the plume during routine operation shown in Fig. 14. Here, we see the extent of the luminous central jet. This feature visibly extends to the same location as the multiple radial velocities shown in Fig. 12. The bright jet feature appears in the same regions where multiple velocity populations appear to be interacting as shown in Figs. 5 and 6. The plume jet appears to be a product of interactions between multiple ion streams. These ions appear to have reasonably well-defined axial velocity components, but broader distributions in their radial velocity components.

It has been suggested by Hruby et al. that the luminous portion of the plume identified as a mixing region may be an ion-acoustic shock [13]. This is consistent with the visual appearance in the plume of a jetlike feature sharply delineated by a highly luminous transition. In Fig. 14, this jet appears to be attached to the nose cone of the Hall thruster. An ion-acoustic shock in this case would result when supersonic xenon ions encounter a potential rise of only a few volts, or less, in the near-field plume. The effect of this shock would be to excite and ionize neutrals, increasing the local plasma density and hence the electron conductivity. It has been suggested that this high-density core may act as an electron conduit between the cathode and anode discharge.

For an ion-acoustic shock to be present in the Hall thruster plume, there should be a jump of several volts in the plasma potential [16]. Evidence for this is not immediately apparent in the LIF velocity data, but may be related to the sudden changes in ion velocity seen near the nose cone in Fig. 12. Immediately beyond the nose cone, the axial velocity is low, but the fluorescence distribution is very broad. Downstream, the ion axial velocity is significantly higher. The appearance of multiple peaks in the axial velocity in Figs. 5 and 6, with accompanying broad radial fluorescence profiles, as shown in Fig. 15, is also consistent with this analysis.

Measurements of the ion flow directed toward the central magnetic pole boron nitride nose cone show that changing the operating parameters varies the impinging ion energy. The velocity measurements may also provide an indication of the relative erosion rate for various portions of the Hall thruster. The most intriguing finding is that lowering the magnetic field while maintaining an essentially nominal anode current increases the divergence of the propellant flow and will likely result in an increase of the erosion rate of the boron nitride nose cone.

The concept of a single velocity, even several distinct velocities, is inadequate, particularly in regions where significant mixing of velocity populations occur. In Fig. 15, we see the fluorescence traces taken at plume centerline 13 mm from the tip of the nose cone (see Fig. 9). The radial fluorescence trace is bimodal with intermediate velocity populations. Although two radial velocities are reported, it is evident that there is in fact a distribution of radial velocities. The same is true for the axial fluorescence trace, albeit to lesser degree.

A more accurate analysis of the true flow dynamics would be to extract a velocity distribution function from each of the fluorescence signals. This would provide a clearer interpretation of the velocity measurements. Because of the lack of the hyperfine spin splitting components of this transition, only an approximate line shape function could be constructed. However, this would be adequate to provide a reasonable indication of the velocity distribution function at each location. Several saturation studies were performed during testing which reveal that the fluorescence signal is not saturated. We plan to continue the analysis of the data to extract velocity distribution functions for later publication.

Another question for which the answer is imperfectly understood is the effect of increasing background pressure on the operation of a Hall thruster. We plan to compare our data to data from a thruster operating at increased background pressure. Comparing spatially resolved velocity distributions for the two cases may provide information on the effects of varying background pressure.

Acknowledgments

The authors are indebted to Lee Johnson of the Jet Propulsion Laboratory and Vlad Hruby of Busek Company for their informative and lively discussions on the nature of Hall thruster plume structure.

References

[1] Fife, J. M., Gibbons, M. R., Hargus, W. A., VanGilder, D. B., Kirtley, D. E., and Johnson, L. K., "3-D Computation of Surface Sputtering and Redeposition Due to Hall Thruster Plumes," *28th International Electric Propulsion Conference*, Electric Rocket Propulsion Society Paper 2003-0136, 2003.

[2] Hargus, W. A., Jr., and Cappelli, M. A., "Laser-Induced Fluorescence Measurements of Velocity Within a Hall Discharge," *Applied Physics B (Lasers and Optics)*, Vol. 72, No. 8, June 2001, pp. 961–969. doi:10.1007/s003400100589

[3] Geisen, H., Krumpelmann, T., Neuschafer, D., and Ottinger, Ch., "Hyperfine Splitting Measurements on the 6265 Å and 6507 Å Lines of Seven Xe Isotopes by LIF on a Beam of Metastable Xe(3P0,3) Atoms," *Physics Letters A*, Vol. 130, Nos. 4–5, July 1988, pp. 299–304. doi:10.1016/0375-9601(88)90614-7

[4] Fischer, W., Huhnermann, H., Kromer, G., and Schafer, H. J., "Isotope Shifts in the Atomic Spectrum of Xenon and Nuclear Deformation Effects," *Zeitschrift für Physik A, Hadrons and Nuclei*, Vol. 270, No. 2, June 1974, pp. 113–120.

[5] Bronstrom, L., Kastberg, A., Lidberg, J., and Mannervik, S., "Hyperfine-Structure Measurements in Xe 2," *Physical Review A*, Vol. 53, No. 1, Jan. 1996, pp. 109–112. doi:10.1103/PhysRevA.53.109

[6] Manzella, D. H., "Stationary Plasma Thruster Ion Velocity Distribution," *30th Joint Propulsion Conference*, AIAA Paper 1994-3141, June 1994.

[7] Pollard, J. E., and Beiting, E. J., "Ion Energy, Ion Velocity, and Thrust Vector Measurements for the SPT-140 Hall Thruster," *Proceedings of 3rd International Conference on Spacecraft Propulsion*, Edited by R. A. Harris, ESA SP-465, 2000.

[8] Beiting, E. J., and Pollard, J. E., "Measurement of Xenon in Velocities of the SPT-140 Using Laser Induced Flourescence," *Proceedings of 3rd International Conference on Spacecraft Propulsion*, Edited by R. A. Harris, ESA SP-465, 2000.

[9] Hansen, J. E., and Persson, W., "Revised Analysis of Singly Ionized Xenon, Xe 2," *Physica Scripta*, Vol. 36, No. 4, 1987, pp 602–643. doi:10.1088/0031-8949/36/4/005

[10] Cedolin, R. J., Hargus, W. A., Jr., Storm, P. V., Hanson, R. K., and Cappelli, M. A., "Laser-Induced Fluorescence Study of a Xenon Hall Thruster," *Applied Physics B (Lasers and Optics)*, Vol. 65, Nos. 4–5, Oct. 1997, pp. 459–469. doi:10.1007/s003400050297

[11] Williams, G. J., Smith, T. B., Gulczinski, F. S., and Gallimore, A. D., "Correlating Laser Induced Fluorescence and Molecular Beam Mass Spectrometry Ion Energy Distributions," *Journal of Propulsion and Power*, Vol. 18, No. 2, 2002, pp. 489–491.

[12] Demtroder, W., *Laser Spectroscopy: Basic Concepts and Instrumentation*, Springer–Verlag, Berlin, 1996.

[13] Hruby, V., Monheiser, J., Pote, B., Rostler, P., Kolencik, J., and Freeman, C., "Development of Low Power Hall Thrusters," *30th Plasma Dynamics and Lasers Conference*, AIAA Paper 1999-3534, 1999.

[14] Miller, M. H., and Roig, R. A., "Transition Probabilities of Xe 1 and Xe 2," *Physical Review A*, Vol. 8, July 1973, pp. 480–486. doi:10.1103/PhysRevA.8.480

[15] Moore, C. E., *Atomic Energy Levels*, Vol. 2, National Bureau of Standards, Washington, D.C., 1958, pp. 113–123.

[16] Chen, F. F., *Introduction to Plasma Physics: Vol. 1 Plasma Physics*, 2nd ed., Plenum Press, New York, May 1990, pp. 297–304.

A. Gallimore
Associate Editor